Coarsening evolution of dendritic sidearms: from synchrotron experiments to quantitative modeling

Neumann-Heyme, H.; Shevchenko, N.; Lei, Z.; Eckert, K.; Keplinger, O.; Grenzer, J.; Beckermann, C.; Eckert, S.;

Coarsening evolution of dendritic sidearms: from synchrotron experiments to quantitative modeling

H. Neumann-Heyme[1*], N. Shevchenko[1*], Z. Lei[1,3], K. Eckert[1,3], O. Keplinger[1], J. Grenzer[1], C. Beckermann[2], S. Eckert[1]

[1]*Helmholtz-Zentrum Dresden-Rossendorf (HZDR), 01314 Dresden, Germany*

[2] *Department of Mechanical and Industrial Engineering, University of Iowa, Iowa City, Iowa 52242, USA*

[3]*TU Dresden, Institute of Process Engineering, 01062 Dresden, Germany*

* Both authors contributed equally, E-mail: h.neumann@hzdr.de, n.shevchenko@hzdr.de

Abstract

The local dynamics of dendritic sidearms during coarsening are studied by combining *in-situ* radiography observations with numerical and analytical models. A flat sample of a Ga-In alloy is partially solidified and then held isothermally in a vertical temperature gradient. The evolving dendritic microstructure is visualized using synchrotron X-ray imaging at the BM20 (ROBL) beamline at ESRF, France. During the coarsening stage, the temporal evolution of the geometrical features of sidebranches is captured by automated image processing. This data is then used to quantify the dynamics of two basic evolution mechanisms for sidebranches: retraction and pinch-off. The universal dynamics of sidearm necks during pinch-off are exploited to determine the product of liquid diffusivity and capillarity length Dd_0, as a parameter that is crucial in the calibration of quantitative models. By employing an idealized phase-field model for the evolution of a single sidebranch, the behavior of selected sidebranches is reproduced from the experiments in a consistent way.

Keywords: Dendritic solidification; microstructure; coarsening; sidearm detachment; X-ray radiography; phase-field model; material properties.

1. Introduction

The solidified microstructure of metal alloys ensues largely from the growth and coarsening of dendrites. During their initial growth into an undercooled melt, dendrites form a characteristic tree-like structure of primary stems and higher-order branches. At a later stage, when the surrounding melt approaches equilibrium, the dendritic structures undergo a slow coarsening process that continuously reduces the number of sidebranches and leads to an increase in the average microstructural length scale. This process is primarily governed by capillarity effects, which cause diffusive material exchange between adjacent structures of different curvature. The coarsening of dendritic structures is characterized by transformation of the side-arm morphology present after growth. It typically proceeds by three mechanisms: (i) retraction of small sidebranches towards their parent stem, (ii) pinch-off or detachment of sidebranches at the narrow neck with the parent stem, and (iii) coalescence of neighboring sidebranches.

The pinch-off of dendrite branches is of particular interest as the resulting dendrite fragments can initiate the growth of equiaxed grains and therefore promote a fine, isotropic microstructure.

The underlying detachment mechanism is a capillarity-driven shape instability that leads to a gradual constriction and collapse of the sidearm neck near the junction with the parent stem.

Over decades, the observation of microstructure formation has been limited to post-mortem analysis of sectioned samples or microscopic imaging in transparent alloys; however, new X-ray sources and innovative procedures for image analysis have dramatically advanced the *in-situ* analysis of evolving microstructures in metal alloys starting around the year 2000 [1,2]. Initial studies involved the radiographic observation of thin samples (2D projections). More recently, microscopic tomography is used to obtain time-resolved, volumetric data [3–6]. Samples are often placed within a temperature gradient, which dictates the direction of growth during cooling. The orientation of the growth with respect to gravity has a strong effect on the strength of buoyancy-driven convection [7]. The resulting solidification conditions affect the dendrite morphology and the tendency to fragment [7–10].

Flat-sample radiographic solidification studies have addressed the effects of composition, cooling rate, gradient magnitude and orientation, and natural or forced convection. Additional information on strains and crystallographic misorientations have been obtained by means of white-beam X-ray topography [11]. Although radiography-based methods allow a relatively large area of the sample to be captured, the limited sample thickness restricts the growth of the dendrites and the flow of the melt compared to bulk sample conditions [12].

X-ray micro-tomography is able to capture volumetric information on the microstructure in small bulk samples. The restrictions in terms of sample size and time resolution are, however, more severe than in radiography. Therefore, tomography has mainly been useful for observing slow processes in small samples, e.g. during dendrite coarsening on a sub-mm scale [3–6]. Nonetheless, the availability of three-dimensional images has enabled the quantification of local and global features of the morphology and their evolution over time.

For metallic alloys, Aagesen et al. [13] investigated the isothermal pinch-off of rod-like solid structures surrounded by liquid melt. Such configurations are prone to a Rayleigh-Plateau like shape instability, where a small local reduction in the cross-section of the structure becomes amplified. This mechanism is caused by the increasing curvature difference between nearby interface regions, which induces diffusional transport through the bulk liquid. Shortly before the structure breaks up, the local curvature of the neck approaches infinity. Due to the strong localization of the neck dynamics and geometry, this process takes on a universal, self-similar behavior. During this stage the geometry of the neck approaches a double cone with an opening angle of 80° and the neck diameter a_N follows

$$a_N(t) = 1.76\big[Dd_0\big(t_p - t\big)\big]^{1/3}, \tag{1}$$

where D is the solute diffusivity in the liquid phase, d_0 the chemical capillary length and t_p the time when the pinch-off occurs. These theoretical predictions were confirmed in [13] by in-situ X-ray tomography of Al-Cu samples during isothermal coarsening.

Recently, Neumann-Heyme et al. [14] performed a computational study of the effects of the initial geometry and cooling rate on the dynamics of sidebranch evolution. The study revealed that sidearms can only pinch off within a limited range of model parameters. Beyond this interval, coalescence or retraction will occur before the sidebranches can detach from the parent stem. The authors confirmed that the pinch-off follows the universal dynamics described in [13] during a short time interval just before pinch-off. These dynamics were found to be independent of model parameters such as the cooling rate.

In the present work, a radiographic analysis of the growth and coarsening of dendrites in a low-melting-point Ga-In alloy is presented using the ROBL beamline (BM20) at the European

2

Synchrotron Radiation Facility (ESRF, Grenoble). The high spatial and temporal resolution achieved in the experiments enables important local geometric features to be accurately captured during the coarsening stage, and their dynamics to be evaluated quantitatively. It is then demonstrated that the measured dynamics can be well reproduced by means of a numerical simulation model of an axisymmetric sidearm, as first developed in [14].

A prerequisite for the implementation of the simulation model is the knowledge of the relevant material parameters, since they select the length and time scale of the interface evolution process. On one hand, the use of a Ga-In alloy in solidification experiments enables simple handling due to its low melting point, but on the other hand, the material properties required for quantitative modeling are highly uncertain. In particular, the product of the diffusion coefficient and capillary length is difficult to measure by conventional means, but is of utmost importance in solidification models. The present study exploits the universality of the pinch-off behavior in the form of Eq. (1) as a tool for the direct determination of Dd_0 based on in-situ observations of the neck dynamics coupled with a simple theoretical analysis. This approach is not restricted to Ga-In, but is also applicable to other alloy systems that have not been thoroughly characterized.

2. Experimental methods and model description

2.1 Experimental setup

The visualization experiments were performed at the ROBL beamline (BM20) at ESRF (Grenoble). The experimental setup, cf. Fig. 1a, used here for the solidification experiments was already employed in previous radiographic investigations carried out by means of a microfocus X-ray tube [15,16].

All experiments were conducted using a low-melting-point hypereutectic Ga–25wt%In alloy that was prepared from gallium and indium of 99.99% purity. The low melting point of the alloy (liquidus temperature 25.7 °C) enables the experiments to be implemented efficiently and flexibly. Furthermore, the Ga–In alloy exhibits a high X-ray contrast between the growing indium dendrites and the interdendritic Ga-rich liquid. A compilation of the material properties is provided in Section 2.4.

The alloy was melted and filled into a Hele-Shaw cell made of Plexiglas with a liquid metal volume of $28 \times 28 \times 0.15$ mm^3. The rectangular observation window determined by the width of the X-ray beam was 20×23 mm^2 in size. The Hele-Shaw cell was cooled at the bottom by means of a Peltier cooler, while a second array of Peltier elements was mounted as a heater on the upper part of the solidification cell. The distance between the heater and the cooler was 19 mm. The simultaneous regulation of the power of both Peltier elements by means of a PID controller unit allowed the cooling rate and the temperature gradient to be adjusted flexibly during the process. Three miniaturized K-type thermocouples (< 0.1 mm) were attached to the lateral surface of the cell to monitor the temperature. The accuracy of the temperature control is ± 0.2 K. In the present experiments, a cooling rate of 0.01 K/s and a temperature gradient of ~ 1 K/mm were applied. The temperature gradient was calculated from the temperature difference measured between the thermocouples T_1 and T_2.

The solidification cell was exposed to a monochromatic X-ray beam with an energy of 28.5 keV. Conventional transmission radiographs were obtained by means of a scintillator that provides a resolution of 2 μm and was coupled to an optical magnifier and a PCO 2000 CCD camera with 2048×2048 pixels (pixel size of 0.34×0.34 μm^2). This equipment leads to a
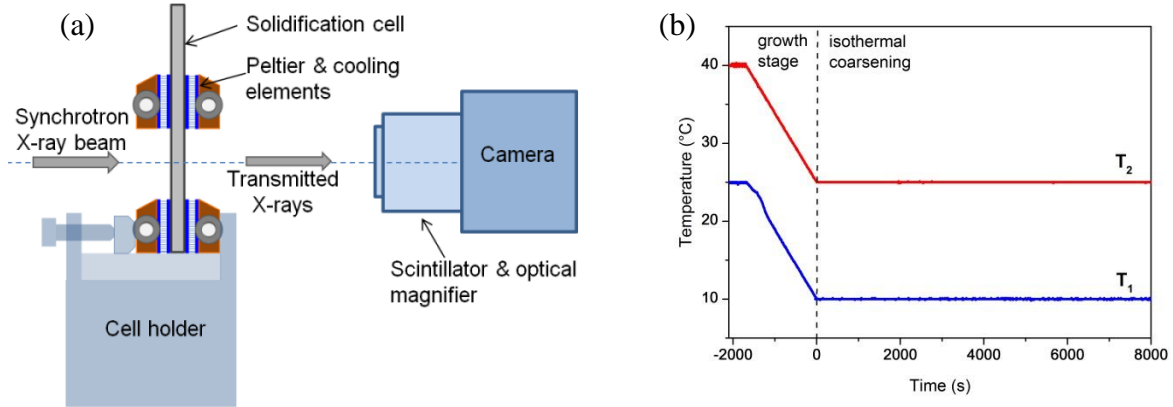
3

Fig. 1. (a) Schematic of the experimental setup showing the arrays of Peltier elements (bottom cooler and top heater). The thermocouples T_1 and T_2 were positioned at distances of 1 and 16 mm, respectively from the upper edge of the cooler. (b) Thermal regime: blue line (T_1) – temperature curve near the cooler; red line (T_2) – temperature curve near the heater.

field of view of about 700×700 µm. The distance between the detector and sample was 20 cm. In order to change the location of the observation window, the position of the solidification cell was manipulated with respect to the X-ray beam by a motorized positioning system with a minimum translation step of 10 µm. Images were acquired at exposure times ranging from 2 to 20 seconds.

Since mainly X-ray scattering experiments have so far been performed on the ROBL beamline, the initially available hardware was not optimized for imaging. Thus, some initial difficulties with the illumination conditions of the sample had to be improved in order to find a good balance between illumination homogeneity, low image noise level, and reasonably low exposure times. Imperfections of the beam line optics caused by the waviness of the mirrors and the monochromator resulted in a horizontal modulation of the beam intensity. However, raw radiography data with even relatively strong artifacts such as shown in Fig. 2a could be successfully analyzed after further image processing whose procedure is explained in the next section 2.2.

The resulting image quality can be seen in Fig. 2b. Here, the image analysis in the area of interest (blue rectangle in Fig. 2b) benefits from high beam intensities and an entirely sufficient signal-to noise ratio. Despite the significant improvement, the illumination is not completely homogeneous over the entire sample showing a slight maximum in the center and decreases towards the upper and the lower edges of the image. The relatively low beam intensity in these side regions causes high image noise along the top and bottom edge of the image such as seen in Fig. 5, which however lays outside the region of interest.

A total of five nominally identical solidification experiments were carried out in the bottom-up configuration (anti-parallel to gravity). Before each experiment the Ga-In alloy was heated to temperatures between 40 and 50 °C for a time period of a few minutes. During this stage the sample was controlled by real-time radiography to ensure that the alloy was homogenously mixed before the cooling process was started. After recording reference images of the completely molten alloy, the cooling of the melt and the image acquisition were initiated. Dark field images and flat field images were also recorded for further data processing. The measured temperatures are shown in Fig. 1b. The sample was first cooled down over a period of 1600 s at a cooling rate of 0.01 K/s. Then, cooling was stopped, leading into an isothermal stage that
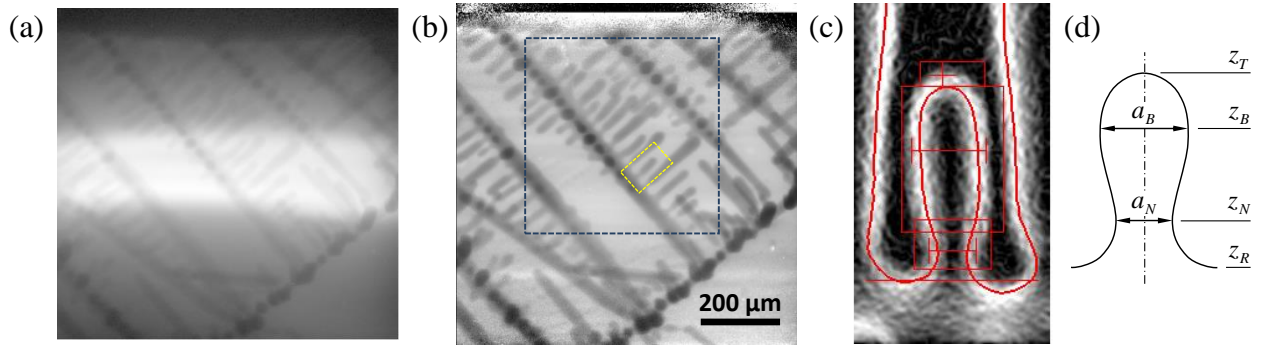
4

Fig. 2. Image processing steps: (a) raw radiogram image using a logarithmic grayscale (exposure time 20 s), (b) after flat-field correction, (c) automated measurement of geometrical sidearm features including the red boxes used to determine the characteristic dimensions of the sidearm, which are explained in the schematic view of a sidearm (d).

was maintained over a period of 150 minutes at a constant temperature difference of 15 K between the heater and cooler.

Note, that due to the presence of a thermal gradient the term 'isothermal' is strictly valid only on the local scale of individual sidebranches. Although the thermal gradient affects the local equilibrium concentration over the sample height, sidearm migration or deflection was not detected during the experiments. Therefore, the temperature was assumed to be locally uniform as far as the evolution of individual sidebranches is considered.

2.2 Data processing

The raw radiography images contained strong artifacts that were caused by spatial and temporal non-uniformities of the X-ray illumination see Fig. 2a. The large-scale structure of the background pattern was almost constant in time, but was subject to significant variations in the vertical direction and fluctuations in intensity.

As a first step in the image processing, the dark image of the camera was subtracted from all frames. To compensate for the temporal intensity changes, the histogram of each frame was stretched to equalize the positions of the bright maximum corresponding to the liquid phase. Thereafter, a flat field correction was performed by first selecting a reference frame of the observation window in the fully liquid state, and then using a smoothed version of this frame that was adapted to the displacement of each individual frame by means of a cross-correlation-based method. The images before and after flat field correction are compared in Figs. 2a and 2b. Note that the illumination distribution in the original image directly affects the local noise level in the corrected image.

The quantitative evaluation of geometrical features of individual sidebranches requires an accurate and robust method to determine the edges of the solid structures in the projected image. For that purpose, the analysis followed two different approaches. First, edge detection was performed by applying a Canny-filter to an image. To obtain robust results the images were pre-smoothed by Gauss-filtering. However, image noise becomes amplified by the derivative operations involved in the edge detection process. Since this leads to reduced sensitivity and artificial thinning of the structures, this strategy was not pursued.

5

The second approach to identify the dendrite contours was based on binarizing the image at a distinct gray value threshold to separate the dark solid structure from the brighter background. This method requires significantly less image smoothing, mitigating the above-mentioned difficulties. However, choosing an appropriate critical threshold value is difficult when the background illumination is non-uniform. Therefore, the edges were identified and measured in multiple steps, where thresholding was performed over progressively smaller sub-regions of the image. In the first step, the edge was approximately identified within a rectangular sub-region that contains the sidearm under consideration (yellow selection in Fig. 2b, red contour in Fig. 2c). This step was needed to compensate for possible translation of the sidearm structure between consecutive frames and to determine the vertical and horizontal extremum points in the sidearm geometry (Fig. 2d). Based on this information, separate sub-regions were identified as indicated by the red rectangles in Fig. 2c. Each of the rectangles contains one of the points or distances to be measured, as shown in Fig 2d. The most crucial part in this method is selecting the threshold value for the outer contour of the solid structure. First, a differential indicator of the edge strength was calculated for the noisy image. Both the gradient magnitude and Laplacian were applied. The resulting field was then averaged over each contour line of constant gray value in the original image ("onion rings"). The maximum among these average values then indicated the gray value threshold that gave the best representation of the edge within the evaluated image region. The advantage of this method is that it tolerates high noise levels, as the disturbed edge information was only evaluated through an integral quantity.

The application of the gradient magnitude slightly underestimates the structure thickness, while a small overestimation was observed when using the image Laplacian. To achieve optimum accuracy, an appropriate threshold value was defined as the average of the gray values that result from these two different edge indicators.

2.3 Single sidearm model

The evolution of sidebranches as observed in the experiment was analyzed by a numerical model of a single sidebranch that is defined by certain geometrical parameters, material properties and thermal conditions. For that purpose, the axisymmetric phase-field model for binary alloys described in [14] was employed. In contrast to [14], where adjacent sidearms are assumed to have the same length, the focus here is on a situation where the sidearm considered is located between two longer sidearms.

By using this simplified axisymmetric model, the sidearm behavior can be described by a small number of essential parameters, which allows for a very efficient and general analysis of the problem. It also provides an intermediate step between a full 3D model and simpler analytical descriptions. The assumptions that are required in the axisymmetric model impose some limits on the accuracy of the predictions, which is discussed in more detail below.

In the model, the temperature is assumed to be constant, and solute diffusion through the liquid melt only occurs due to differences in curvature between different regions of the solid-liquid interface, which is typical for coarsening processes (melt supersaturation is negligibly small). The initial geometry consists of the idealized sidearm shape shown in Fig. 3a. This geometry captures the essential geometrical properties of a simple dendrite sidearm: its radius R, length l, and characteristic lateral distance λ_r to its neighbors.

The present model assumes quasi-stationary diffusion, since the motion of the interface is slow compared to the relaxation of the diffusion field. This condition is satisfied once the melt concentration approaches equilibrium and the characteristic geometric length scale (in the

6

present case R) is much greater than the capillary length, i.e. $d_0/R \ll 1$. Under these circumstances, the usual free boundary problem of isothermal, binary alloy solidification can be significantly simplified [14]. First, a scaled supersaturation is introduced as

$$U = \frac{(c - c_l^0)R}{\Delta c d_0},$$

(2)

where c, c_l^0, Δc, and d_0 are the solute concentration, the initial concentration of the liquid, the miscibility gap, and the capillary length, respectively. For a linearized phase diagram the miscibility gap can be expressed by $\Delta c = c_l^0(1 - k)$, where k is the partition coefficient. Further relationships between these parameters and the specific conditions in the present experiment are discussed later in Section 2.4. Length and time are scaled by

$$\xi_x = R \quad \text{and} \quad \xi_t = R^3/Dd_0,$$

(3)

respectively. Solute diffusion in the melt is then governed by

$$\nabla^2 U = 0,$$

(4)

whereas diffusion in the solid phase is neglected. At the interface, mass conservation and the Gibbs-Thomson condition are given by

$$V_n = -\partial_n U|_i^+$$

(5)

and

$$U|_i = -\kappa,$$

(6)

respectively, where V_n is the interface velocity in the normal direction n, and κ is the local sum of the principal curvatures of the interface. In these definitions n is pointing towards the liquid phase and κ is positive for a concave solid. The subscript i and superscript $+$ denote the interface location and positive normal direction, respectively.

It can be seen that the dimensionless model given by Eqs. (4)–(6) is independent of any material parameters. The model is solely a function of the initial geometry, as shown in Fig. 3a, and the assumption of equilibrium between the solid and liquid phases, which corresponds to an initial value of $U = 0$ throughout the domain.

The model domain is limited in the longitudinal direction by no-flux boundary conditions at $z = 0$ and $z = \lambda_z$, respectively, as indicated in Fig. 3a. In contrast to the previous work [14], the radial boundary at $r = \lambda_r$ is defined by a fixed value for U that corresponds to the presence of an interface of a given curvature via the Gibbs-Thomson relation, Eq. (6). This models a sidearm that is situated between significantly longer arms, where the tip interacts with the lateral, cylinder-like surfaces of the neighboring sidearms. The neighboring sidearms are assumed to have the same radius R as the central arm that is being modelled. Images of the real microstructure obtained from the experiments justify this assumption, in particular for the case that is referenced by numerical modeling in Section 3.2.2.

Furthermore, some issues need to be addressed that arise from the assumption of rotational symmetry in the model. Figure 3b schematically compares the geometry of the axisymmetric model (red line) with the three dimensional sidearm geometry found in the experiment (cf. Fig. 7 in Section 3.2). The full and dashed black lines represent the vertical sections parallel and perpendicular to the main stem, respectively. It is seen, that the root region of the sidearm appears concave in the parallel section and convex in the perpendicular section. The averaging over both curvatures leads to a nearly flat shape of the root region similar to that assumed in
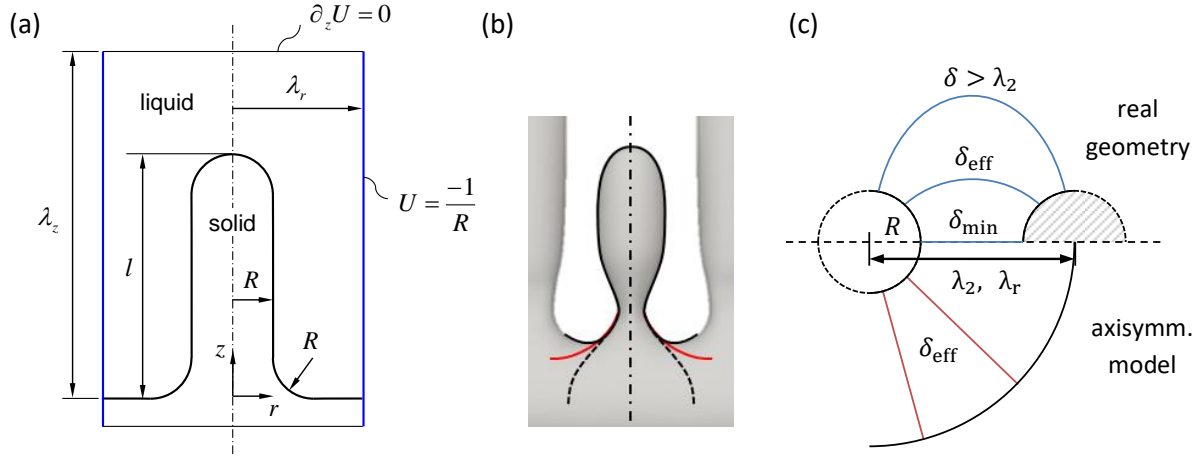
7

Fig. 3. (a) Definition of the initial geometry and domain boundaries; (b) root region geometry of the sidearm: axisymmetric model (red line), vertical sections of the real geometry parallel (full black line) and perpendicular (dashed black line) to the main stem; (c) top view of the diffusion paths between the model sidearm (left) and its right neighbor (the mirrored left neighbor is not shown).

the present model (red line), which therefore provides a reasonable approximation of the real sidearm geometry.

The second aspect concerns the non-axisymmetric diffusion between the sidearms. Fig. 3c shows a schematic top view of the lateral mass flux between the modeled sidearm and its neighbor (hatched area), where the upper half represents the real geometry and the lower half the axisymmetric model. The highest flux will usually occur for the path of minimum length, which for the real geometry is $\delta_{min} = \lambda_2 - 2R$. The flux then decreases with increasing length of the outward bending flux paths. The total flux can be expressed by an effective path length δ_{eff} which is approximately $\lambda_2 - R$. It can be seen, that the choice of $\lambda_r = \lambda_2$ for the lateral spacing of the axisymmetric model will result in an equivalent path length of $\delta_{eff} = \lambda_r - R$.

There are no specific requirements for the longitudinal distance λ_z. However, a value of $\lambda_z > l + \lambda_r$ should be chosen to ensure that the condition of "long neighbors" is met and to avoid any effect of the upper domain boundary on the sidearm dynamics.

2.4 Material properties of Ga-In

An important prerequisite for applying the coarsening model to the actual experiments is the knowledge of both the characteristic length scale, identified here as the initial sidearm radius R, and the product of the diffusion coefficient and the capillary length, Dd_0, cf. Eq. (3). Whereas $2R$ can be measured directly from the experimental images, the parameter combination Dd_0 is much more difficult to determine due to its dependence on both the temperature range ΔT and the solute concentration c.

In the present study, the product Dd_0 is obtained using two different methods. In the first method, the relevant material data for Ga-In alloys are compiled through an extensive analysis of the literature. This procedure has the disadvantage that parameters collected from different sources could show significant scatter or do not exactly fit the experimental conditions. In the second approach, the product Dd_0 is inferred from measurements of appropriate dynamical features within the coarsening experiment.

8

While the second method is explained in Section 3.2.1, the remainder of this section explains how the property data were obtained from the literature. The equilibrium phase diagram for Ga-In is displayed in Fig. 4. Note, that the phase diagram is shown for the In concentration, which is related to the solute (Ga) concentration by $c' = 1 - c$. At an initial concentration of $c'_0 = 25$ wt% In and conditions near phase equilibrium, the liquid concentration $c_l^{0'}$ is close to the eutectic value c'_e. Note that due to the significant undercooling tendency of Ga [17], the formation of the eutectic phase is delayed until the temperature drops ~ 30 K below the eutectic temperature T_e. Usually, the solidification structure remains purely dendritic around the eutectic point.
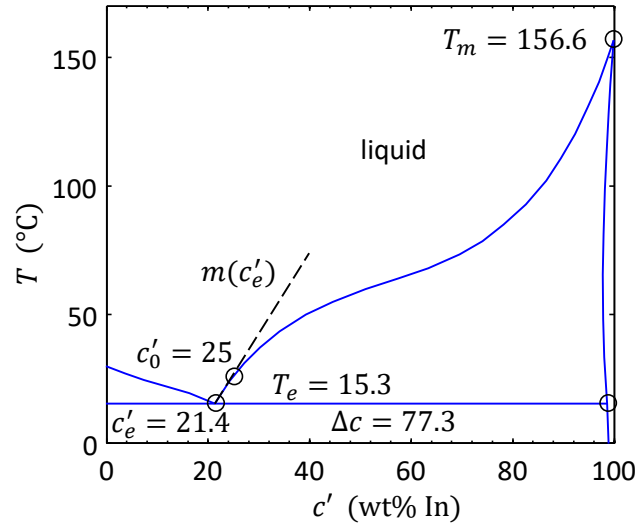

Fig. 4. Equilibrium phase diagram for the Ga-In system [16] illustrating some quantities presented in Table 1.

In Table 1, all relevant data from the phase diagram are summarized together with additional material parameters that are necessary to determine the value of Dd_0. The properties are evaluated at the eutectic temperature T_e because the local temperature during the experiment in the center of the observation window is close to T_e.

Since no direct measurements for the interface energy γ_{SL} between the solid and liquid phase were found in the literature, γ_{SL} was estimated from the liquid-vapor interface energy γ_{LV} according to [18]. The latter quantity can be measured by well-established techniques. Note that in the case of alloys, this value may also depend on the concentration, but this is not taken into account here due to missing data.

The solute diffusion coefficient D in the liquid is a parameter that is generally difficult to measure directly and is often affected by convection. In general, D can show a strong dependency on the solute concentration, which is not always clearly stated in the literature. The present analysis follows the work of Savintsev et al. [19]. To our best knowledge, this is the only study available on the diffusion coefficient in liquid Ga-In alloys. In Ref. [19], data measured in contact melting experiments is fitted to an analytical diffusion model based on the regular solution approximation. To obtain a relationship between the diffusion coefficient D and the concentration C' in at% indium, the parameters provided in their paper are inserted into Eq. (2) of their paper. This allows the following equation to be deduced for the concentration dependence of D:

9

$$D(C') = D_{\text{In}}(1 + 1.3C')[1 - 5C'(1 - C')], \tag{7}$$

where $D_{In} = 0.86 \times 10^{-9}$ m^2/s is the self-diffusion coefficient of indium. In contrast to frequently studied alloys such as Al-Cu, the diffusion coefficient in liquid Ga-In shows a strong dependence on concentration. According to Eq. (7), D doubles when the concentration is reduced by 10 at% relative to C'_e. The diffusion coefficient in Table 1 is evaluated at the eutectic point using a value of $C' = C'_e = 16.5$ at% In (24.5 wt% In) as given in [19]. This value is chosen for consistency with the original phase diagram data associated with Eq. (7) even though it is slightly different from the eutectic concentration reported in Fig. 4. The analysis by Savintsev et al. [19] was carried out near the eutectic temperature, which also corresponds to

Table 1. Material properties for a Ga-In alloy

Parameter	Symbol	Value	Units	Relation	Ref.
Melting temperature [a]	T_m	429.75	K	from phase diagram, Fig. 4	[17]
Eutectic temperature	T_e	288.45	K	from phase diagram, Fig. 4	[17]
Liquidus slope [b]	m	2.97	K/wt%	from phase diagram, Fig. 4	[17]
Miscibility gap [b]	Δc	77.3	wt%	from phase diagram, Fig. 4	[17]
Molar mass [a]	M	114.82	g/mol	-	[25]
Liquid density [a), b)]	ρ	7126.1	kg/m^3	$7030 - 0.68\,(T - T_m)$	[25]
Latent heat at T_m [a]	L_m	3270	J/mol	-	[25]
Interface energy liquid/vapor [a), b)]	γ_{LV}	0.5687	J/m^2	$0.556 - 9 \times 10^{-5}(T - T_m)$	[25]
Interface energy solid/liquid [a), b)]	γ_{SL}	0.0867	J/m^2	$0.1525\,\gamma_{LV}$	[18]
Gibbs-Thomson coefficient [b]	Γ	1.837×10^{-7}	K m	$\gamma_{SL}T_m/(L_m\rho/M)$	[24]
Capillary length [b]	d_0	0.80×10^{-9}	m	$\Gamma/(|m|\Delta c)$	[24]
Diffusion coefficient in liquid [b]	D	0.325×10^{-9}	m^2/s	see Eq. (7)	[19]

a) of indium
b) at the eutectic point, i.e. $T = T_e$ (or $c = c_e$)

the temperature in the experiments of the present study. Therefore, any dependence of D on temperature is taken into account here.

The data of Table 1 result in a value of

$$Dd_0 = 0.26 \ \mu\text{m}^3\text{s}^{-1}. \tag{8}$$

Given the very approximate nature of the above method, we are not able to provide a meaningful estimate of the uncertainty in the above value of Dd_0.

In Section 3.2.1 we compare this result with the value obtained by the second approach, which determines this quantity directly from the experimental data. It is shown that only the latter value, which is smaller than the one in Eq. (8) by a factor of more than two, enables a consistent prediction of sidearm evolution using the present coarsening model.

3. Results and discussion

3.1 General observations

Following the experimental procedure described in Section 2.1 the sample was cooled down and observations were carried out in a rectangular observation window of 0.7×0.7 mm^2, the lower edge being 2 mm above the bottom Peltier cooler. The first dendrites became visible at this location when the temperature reached 14.9 °C. This corresponds to an approximate dendrite tip undercooling of 10.8 K. Figure 5a shows a dendrite emerging from a single grain

at the bottom right-hand corner of the observation window. In contrast to the liquid melt, the solid phase consists of almost pure indium (see phase diagram, Fig. 4), which causes the dendrite to appear dark due to its high X-ray attenuation. The crystallographic orientation of the dendrite is essentially random despite the presence of a temperature gradient. The velocities of the dendrite tips were observed to range from 30 to 48 µm/s. They showed significant fluctuations that are likely caused by buoyant flow instabilities associated with the current experimental setup. These convective effects are characteristic of bottom-up solidification where the rejected solute (Ga) causes the melt close to the dendrites to be lighter than the melt near the top of the cell. They have been reported in similar experiments in the past [7,15,16].
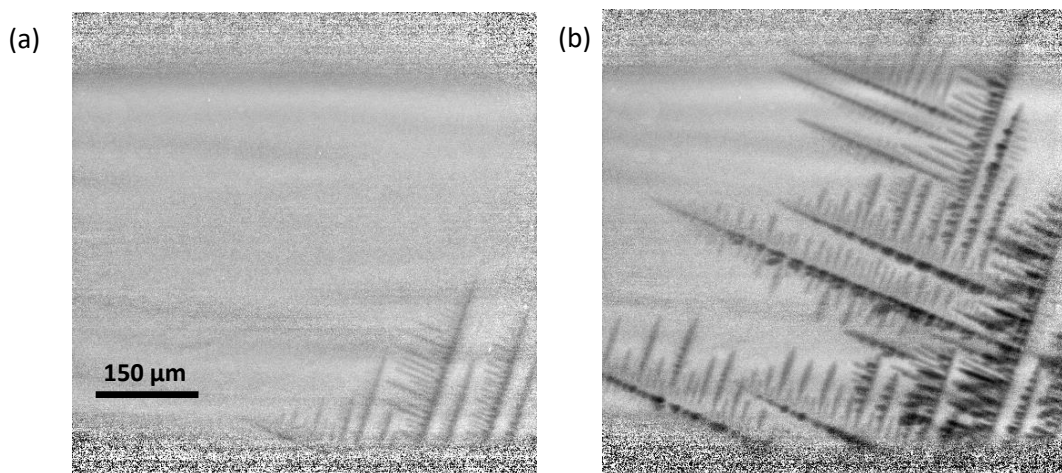

Fig. 5. Radiographs (exposure time 2 s) of the growing dendrite at different times according to Fig. 1b: (a) −410 s, (b) −386 s (the lower edge of the observation window is located 2 mm above the bottom cooler).

During the early solidification stage, an average secondary arm spacing of $\lambda_2 = 10$ µm was measured throughout the sample (Fig. 5b). In the present study, no dendrite fragmentation was detected during the growth stage.

After the end of cooling, dendrite growth stops at a height of about 7 mm from the bottom cooler. While maintained in a constant temperature gradient, the dendrite structure continues to evolve through isothermal coarsening. Convection effects quickly disappear due to viscous effects and the absence of strong concentration gradients during this stage.

To study the temporal evolution of the sidearm morphology during the isothermal holding phase, a magnified section of the image, located 6.5 mm above the bottom cooler, was selected. In this region, the crystallographic orientations of the dendrites are well aligned with the sample plane, which can be deduced from the ninety-degree angle between the sidearms and the main trunk as well as from the distinct spot-like projection of the perpendicular sidearms. These conditions are favorable for geometrical analysis as the dendrite arms in the sample plane appear at their real length and overlapping structures are minimized. Although dendrites are confined in the thickness direction of the sample, the sample gap width is significantly larger than the diameters of the observed structure. Therefore, the effect of the confinement can be neglected for sidearms that evolve in the sample plane.

Figure 6 presents three X-ray images acquired at different times, showing the region of the dendrite selected for the quantitative measurements of the sidearm evolution. Detailed
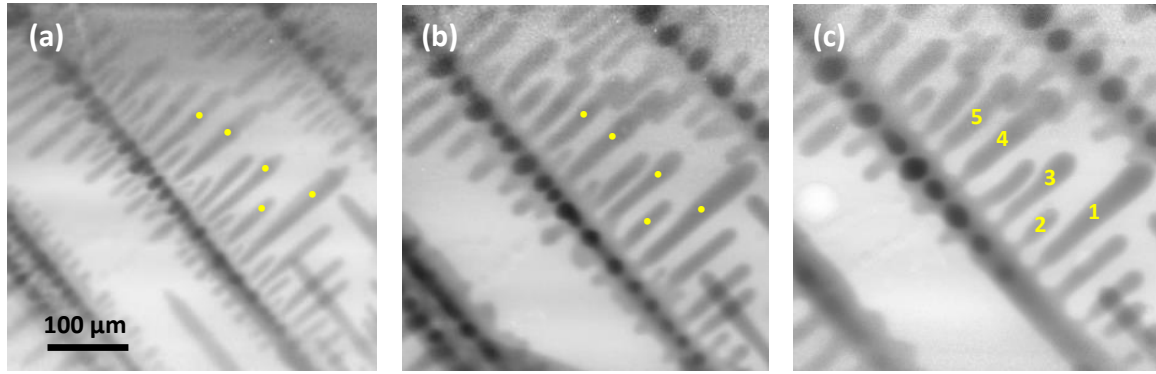
11

Fig. 6. X-ray images showing the development of secondary dendrite branches during the isothermal holding phase (t = 0 corresponds to the start time of the isothermal phase): (a) 100 s, (b) 1950 s, and (c) 4750 s [sidebranches for quantitative evaluation are labeled in (c) and marked by dots in (a) and (b)].

measurements of morphological parameters were performed for the five sidearms marked in Figs. 6a–c. The observations were carried out over a period of 8000 s after the onset of the isothermal phase.

During isothermal holding phase, the sidebranch structure coarsens continually, resulting in the secondary dendrite arm spacing λ_2 to increase from approximately 10 µm to a mean value of 85 µm after 2700 s. At the same time, the diameter of the primary trunk increases from 24 to 35 µm for the central dendrite stem in Fig. 6. While coalescence occurs rarely for the low solid volume fraction, which is approx. 0.1 in the area of investigation, sidearm retraction and occasional pinch-off where identified as the major coarsening mechanisms. Note, that in the present study the solid fraction is not a necessary quantity, because the proximity of the coarsening interfaces is known from the experimental distance measurements. The solid fraction however becomes an essential parameter when the case of net solidification is considered [14,20]. The following section considers the observed mechanisms of sidearm evolution and their dynamics in more detail.

3.2. Sidearm evolution during coarsening

Sidearm 2 in Fig. 6c is now selected for further analysis because it features both retraction and pinching. Figure 7 shows Sidearm 2 at three different times until pinch-off. The shape of the sidearm calculated by the numerical model is superimposed as a yellow line. Very good agreement can be observed between the measured and predicted sidearm shapes. In Fig. 8 the geometrical dimensions of Sidearm 2 (see Fig. 2d for their definition) are plotted against time relative to the pinch-off time, t_p. The pinch-off time t_p is defined as the earliest time when movement of the fragment relative to the parent dendrite was detected. The experimental data are plotted as red circles and are discussed in the following. The results obtained from the numerical model (black lines) are discussed further in Section 3.2.2.

Under isothermal coarsening conditions, where the overall volume of solid material remains constant, the observed melting and deposition processes can be interpreted as solid material being transferred from regions of higher to regions of lower curvature. The retraction of the tip is caused by its higher curvature compared to the interfaces of the adjacent sidearms. In contrast, the longer arms Sidearms 1, 4, and 5 in Fig. 6 are growing due to the presence of smaller remelting sidearms nearby.
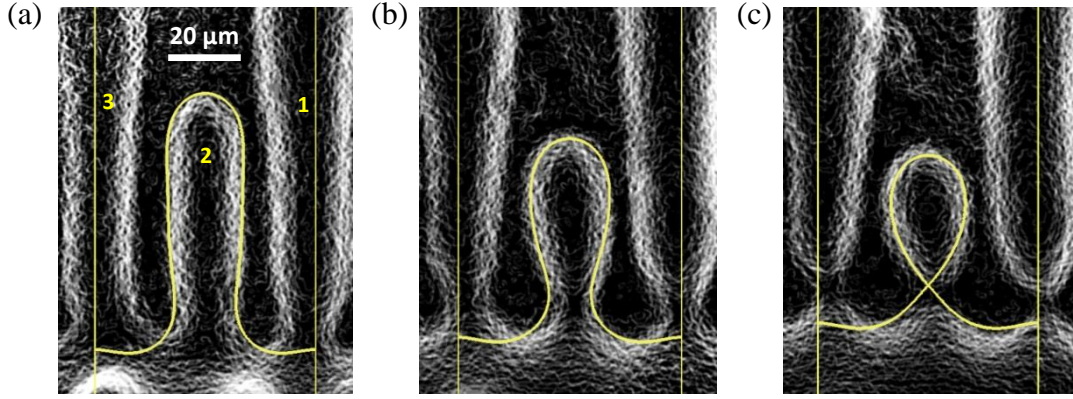
12

Fig. 7. Comparison of the evolution of Sidearm 2 between experiment and numerical simulation (yellow lines) at (a) $t_p - 5380$ s, (b) $t_p - 1670$ s, and (c) the pinch-off time t_p, where $t_p = 7660$ s. Experimental images are displayed as the magnitude of the intensity gradient for better visibility of the geometric contours.
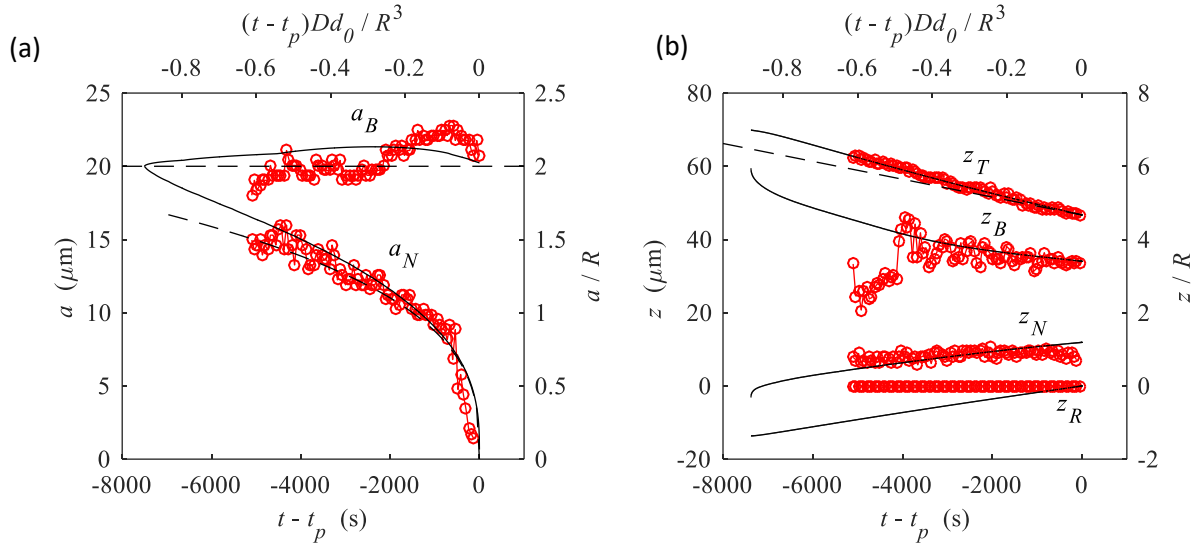

Fig. 8. Evolution of geometrical parameters for Sidearm 2; red circles: experimental measurements, black lines: numerical model; bottom and left axes are in physical units, top and right axes in scaled units, respectively; (a) bulge and neck diameter [dashed line in a_B: reference radius $R = a_B/2$ for the model, dashed line in a_N: fit according to Eq. (1)]; (b) vertical positions for tip, bulge, neck and root [dashed line in z_T: analytical model Eq. (10)].

As can be seen in Fig. 8b, the longitudinal tip coordinate z_T of Sidearm 2 decreases at a constant rate, indicating that the conditions driving the retraction of the sidearm do not change with time. This allows the tip position measurements to be compared with a simple analytical retraction model (dashed line) that is presented in Section 3.2.2.

At the same time as the sidearm tip retracts, constriction of the neck can be observed. The neck is defined as the narrow connection between the sidearm and the parent stem. This remelting process is driven by the difference between the high curvature of the neck and the low curvature of the nearby root or stem region. Figure 8a shows that the decrease in the neck diameter a_N is very rapid when the pinch-off time is approached. The resulting fragment is carried away by gravitational forces and melt motion.

13

During the entire process, the longitudinal position of the neck z_N remains almost constant relative to the root coordinate z_R, as shown in Fig. 8b. The longitudinal position of the sidearm bulge z_B (maximum diameter of the sidearm, see Fig. 2d) generally decreases. The fluctuations in z_B prior to the decrease can be attributed to the difficulty of identifying the location of the maximum bulge diameter at an early stage. The bulge diameter a_B plotted in Fig. 8a remains approximately constant, except for small fluctuations near the pinch-off time.

3.2.1 Quantitative evaluation of the pinch-off dynamics

The temporal evolution of the neck diameter a_N during coarsening under isothermal conditions is predicted to approach the self-similar behavior described by Eq. (1) as $t \rightarrow t_p$. This equation is tested here using the present measurements. It contains the product Dd_0 as the only material parameter. This product is constant for an alloy of a given composition and temperature. The measured neck diameters for all five sidearms identified in Fig. 6c are plotted in Fig. 9a. By including measurements from multiple sidearms, statistical errors are greatly reduced. Fig. 9a shows that in accordance with Eq. (1) the measured neck diameter indeed evolves with the cube root of time. This self-similar behavior is already displayed up to 6000 s before pinch-off, when the neck diameter is still 15 μm. Data for a_N less than about 6 μm (gray circles in Fig. 9a) must be excluded because of measurement uncertainties due to insufficient image contrast against the background noise in the images.
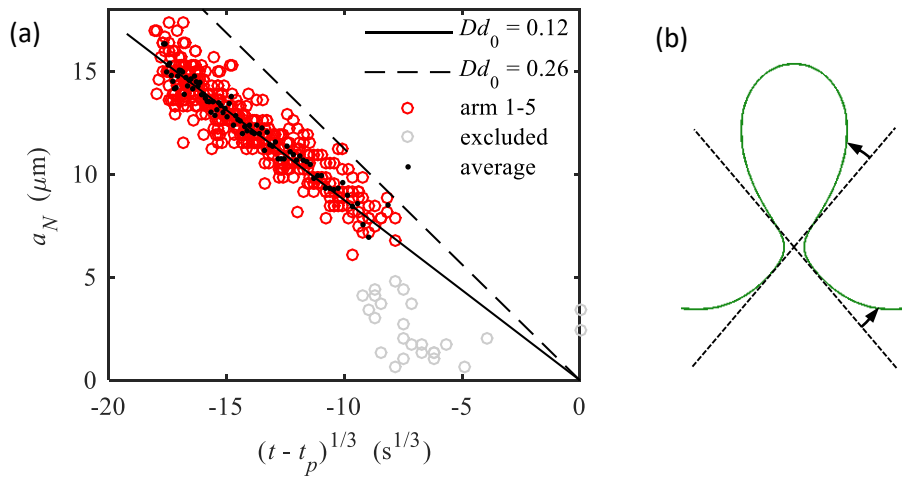

Fig. 9. (a) Neck diameter of five sidearms (see Fig. 6c) vs. the non-linear time; results from Eq. (1) are drawn for $Dd_0 = 0.122 \ \mu m^3 s^{-1}$ (solid line) and $Dd_0 = 0.26 \ \mu m^3 s^{-1}$ (dashed line), respectively; (b) side view of the pinching region: actual axisymmetric sidearm (solid line) vs. asymptotic shape of the self-similar approximation (dashed line).

By fitting the measured data for $a_N > 6$ μm to Eq. (1), the following value for the product Dd_0 is obtained

$$Dd_0 = 0.122 \pm 0.0026 \ \mu m^3 s^{-1}, \tag{9}$$

corresponding to an uncertainty of 2.1 % for a 95 % confidence interval. For comparison, the neck diameter predicted by Eq. (1) using Eq. (8) for the product Dd_0 is also plotted in Fig. 9a. Recall that Eq. (8) is based on estimates of material properties found in the literature.

14

Considerable discrepancies with the present measurements can be observed. The two values of the product Dd_0 given by Eqs. (8) and (9) differ by approximately a factor two. Given the significant uncertainties associated with the estimation of the material properties in Section 2.4, such a difference is quite plausible.

The rate at which the neck collapses is determined by the interface curvature differences and length of the diffusion paths between the neck (maximum curvature) and adjacent regions of lower curvature. Shortly before pinch-off the region around the neck attains a self-similar geometry [13] that closely resembles a hyperbola of revolution. The pinch-off process is self-similar because the neck retains a constant shape when scaled by a time-dependent factor, as given by Eq. (1). In the self-similar regime, the contour of the neck approaches straight lines, as shown by the dashed lines in Fig. 9b. However, the actual neck shape (solid lines in Fig. 9b) at large times before pinch-off is different from the self-similar shape. As indicated by the arrows in Fig. 9b, the interface is more convex towards the sidearm bulge region and more concave towards the root region. Therefore, the pinching tendency above the neck is reduced due to higher curvatures and longer diffusion distances. Conversely, the pinching tendency below the neck is enhanced due to lower curvatures and shorter diffusion distances. These effects tend to compensate for each other, even at times far before pinch-off. As a result, the evolution of the neck diameter follows the predictions of the self-similar model for much longer times than would be expected based on the model assumptions. These arguments are further confirmed next when the measurements are compared to the numerical sidearm model.

3.2.2 Modeling results

The numerical model of a single axisymmetric sidearm introduced in Section 2.3 was used to simulate the retraction and pinch-off of Sidearm 2. The basic model parameters that set the length and time scales in Eq. (3) are the value of Dd_0, which was taken from Eq. (9), and the initial sidearm radius, which was approximated as $R = 10\,\mu m$ from the measured bulge diameter data in Fig. 8a. The other model parameters relate to the initial geometry (Fig. 3a) and were chosen as $\lambda_r = 3R$, $l = 8.2R$, and $\lambda_z = 20R$. While these values for the model parameters produce good agreement with the experiment, as already shown in Figs. 7 and 8, they require some additional discussion.

As already argued in Section 2.3, the lateral spacing λ_r can be approximated as the secondary dendrite arm spacing λ_2, which is $\approx 3R$ (30 μm) for the scenario considered in Fig. 7. This choice is corroborated by the good agreement between the measured and predicted tip position z_T in Fig. 8b, because the retraction rate $\dot{z}_T$ depends strongly on λ_r. The initial sidearm length l is deduced from a linear extrapolation of the experimental z_T data in Fig. 8b to an earlier time. As can be seen in Fig. 8, the simulation is started at an earlier time than the experimental shape measurements. This leading time is required for the "artificial" initial model geometry to adopt a more natural shape of continuous curvature. Finally, the height of the computational domain λ_z is simply chosen large enough to prevent any influence of the upper boundary of the simulation domain.

Examining in more detail the results in Fig. 8, it is apparent that the evolution of the neck diameter a_N predicted by the numerical model agrees not only with the measured data, but also with the analytical result given by Eq. (1). The growing disagreement between the numerical model and Eq. (1) at scaled times smaller than about -0.6 can simply be attributed to the need for the initial geometry of the numerical model to evolve to a more natural shape. Nonetheless, the results of the numerical model confirm that Eq. (1) is valid at times far before the self-similar pinch-off regime is reached.

15

Some disagreement can be observed in Fig. 8b between the measured and predicted longitudinal positions of the sidearm neck z_N and root z_R. The experimental data for z_R are constant per definition, because this position was used as a reference point for the local coordinate system. However, additional examination of the experimental images, not shown here for conciseness, confirmed that the distance between the sidearm root and the center of the parent stem was nearly constant during the measurement period. The upwards migration of the root and neck positions in the numerical model can be explained by remelted material from the neck filling up the bottom region representing the main stem. In reality, such remelted material can deposit along the entire circumference of the parent stem. The present axisymmetric model cannot reproduce this effect.

Fig. 8b shows excellent agreement between the measured and predicted arm length z_T variations. This quantity is also predicted by an analytical sidearm retraction model developed by Kattamis et al. [21]. This model considers a cylindrical sidearm of radius R_a that is located between two longer sidearms of radius R_b. Assuming that R_a and R_b are constant, the sidearm tip retraction rate is given by

$$\dot{z}_T = \frac{-2Dd_0}{R_a}\left(\frac{2}{R_a} - \frac{1}{R_b}\right). \tag{10}$$

The assumptions of this model appear to be satisfied for Sidearm 2 in the experiment. As in the numerical model, Dd_0 is taken from Eq. (9) and $R_a = R_b = R$. As shown by the dashed line in Fig. 8b, the analytical model by Kattamis et al. [21] is in reasonable agreement with both the experiment and the numerical model.

A parametric study was performed to address the impact of the lateral spacing on the retraction rate. It revealed that if the gap between the sidebranch and its neighbors is much smaller than its length, remelting of the tip is primarily caused by its interaction with the neighboring sidearm stems. Otherwise, if the sidearm is sufficiently short compared to the lateral gap, its interaction becomes dominated by the presence of the low-curvature root region. While in the present case the lateral flux still dominates, the longitudinal component towards the root region is already relevant. This might explain why the simple model in Eq. (10) underestimates the retraction rate, as it does not include the latter effect.

4. Conclusions

The present study has investigated the isothermal coarsening dynamics of dendritic sidearms. It is shown that synchrotron radiography of a thin sample is a highly suitable experimental technique for studying the interface dynamics of dendritic structures in metallic alloys. It offers high spatial and temporal resolution over a relatively large sample area. Compared to similar tomographic measurements [22], it is much simpler and requires the processing of 2D images only. The present measurements provide real-time *in-situ* data on two phenomena that are of great importance in coarsening of dendrites: sidearm retraction and pinch-off.

The experimental data show that the sidearm neck diameter evolves with the cube root of time over a period that is much longer than anticipated from a previously developed self-similar analytical model [13]. This model is strictly valid only very close to the pinch-off time. Because measurements of multiple sidearms collapse to the same curve, this behavior is universal and insensitive to the exact initial geometry and the surroundings of a sidearm. Furthermore, the fact that the neck diameter varies with the cube root of time indicates that in the present experiments melt convection is not important during the coarsening phase [23]. This is not

surprising considering the thin sample geometry and the presence of a finely dispersed solid structure. By fitting the neck diameter data to the analytical expression, the material parameter Dd_0 can be determined in a simple and accurate manner. The parameter Dd_0 is needed in numerous models of solidification and coarsening [20,24], but is difficult to obtain from published property data. The knowledge of Dd_0 for the present Ga-In alloy suggests that this low-melting alloy, displaying a high X-ray contrast, will be highly useful for future solidification and coarsening studies.

The measured evolution of the dendrite sidearm shape is found to agree very well with the predictions from a relatively simple axisymmetric numerical model. This is true for not only the neck diameter but also for the sidearm tip retraction rate and other geometrical features. Hence, the present experiments provide conclusive validation of the numerical model. As we recently demonstrated [14], the model is simple enough that it can be used to perform a wide range of parametric studies related to coarsening and fragmentation of dendritic structures. Complementary studies using a more realistic 3D modeling of the individual sidebranch geometry and improved material characterization are desirable and currently underway.

Acknowledgements

References

[1] H. Nguyen-Thi, L. Salvo, R.H. Mathiesen, L. Arnberg, B. Billia, M. Suery, G. Reinhart, On the interest of synchrotron X-ray imaging for the study of solidification in metallic alloys, C R Phys. 13 (2012) 237–245.

[2] R.H. Mathiesen, L. Arnberg, F. Mo, T. Weitkamp, A. Snigirev, Time resolved X-ray imaging of dendritic growth in binary alloys, Phys Rev Lett. 83 (1999) 5062–5065.

[3] L.K. Aagesen, J.L. Fife, E.M. Lauridsen, P.W. Voorhees, The evolution of interfacial morphology during coarsening: A comparison between 4D experiments and phase-field simulations, Scr. Mater. 64 (2011) 394–397.

[4] N. Limodin, L. Salvo, E. Boller, M. Suery, M. Felberbaum, S. Gailliegue, K. Madi, In situ and real-time 3-D microtomography investigation of dendritic solidification in an Al-10 wt.% Cu alloy, Acta Mater. 57 (2009) 2300–2310.

[5] S. Terzi, L. Salvo, M. Suery, A.K. Dahle, E. Boller, Coarsening mechanisms in a dendritic Al–10% Cu alloy, Acta Mater. 58 (2010) 20–30.

[6] S. Shuai, E. Guo, A.B. Phillion, M.D. Callaghan, T. Jing, P.D. Lee, Fast synchrotron X-ray tomographic quantification of dendrite evolution during the solidification of Mg-Sn alloys, Acta Mater. 118 (2016) 260–269.

[7] J.W. Gibbs, D. Tourret, P.J. Gibbs, S.D. Imhoff, M.J. Gibbs, B.A. Walker, K. Fezzaa, A.J. Clarke, In situ X-Ray observations of dendritic fragmentation during directional solidification of a Sn-Bi alloy, JOM - J. Miner. Met. Mater. Soc. 68 (2016) 170–177.

[8] D. Ruvalcaba, R.H. Mathiesen, D.G. Eskin, L. Arnberg, L. Katgerman, In situ observations of dendritic fragmentation due to local solute-enrichment during directional solidification of an aluminum alloy, Acta Mater. 55 (2007) 4287–4292.

17

[9]   S. Boden, B. Willers, S. Eckert, G. Gerbeth, Observation of dendritic growth and fragmentation in Ga-In alloys by X-ray radioscopy, Int J Cast Met. Res. 22 (2009) 30–33.

[10] G. Zimmermann, C. Pickmann, M. Hamacher, E. Schaberger-Zimmermann, H. Neumann-Heyme, K. Eckert, S. Eckert, Fragmentation-driven grain refinement in directional solidification of AlCu10wt-% alloy at low pulling speeds, Acta Mater. 126 (2017) 236–250.

[11] G. Reinhart, A. Buffet, H. Nguyen-Thi, B. Billia, H. Jung, N. Mangelinck-Noel, N. Bergeon, T. Schenk, J. Haertwig, J. Baruchel, In-Situ and real-time analysis of the formation of strains and microstructure defects during solidification of Al-3.5 wt pct Ni alloys, Met. Mater Trans A. 39A (2008) 865–874.

[12] N. Bergeon, R. Trivedi, B. Billia, B. Echebarria, A. Karma, S. Liu, C. Weiss, N. Mangelinck, Necessity of investigating microstructure formation during directional solidification of transparent alloys in 3D, Adv. Space Res. 36 (2005) 80–85.

[13] L.K. Aagesen, A.E. Johnson, J.L. Fife, P.W. Voorhees, M.J. Miksis, S.O. Poulsen, E.M. Lauridsen, F. Marone, M. Stampanoni, Pinch-off of rods by bulk diffusion, Acta Mater. 59 (2011) 4922–4932.

[14] H. Neumann-Heyme, K. Eckert, C. Beckermann, Dendrite fragmentation in alloy solidification due to sidearm pinch-off, Phys Rev E. 92 (2015).

[15] S. Boden, S. Eckert, B. Willers, G. Gerbeth, X-ray radioscopic visualization of the solutal convection during solidification of a Ga-30 wt pct In alloy, Met. Mater Trans A. 39A (2008) 613–623.

[16] N. Shevchenko, S. Boden, G. Gerbeth, S. Eckert, Chimney formation in solidifying Ga-25wt pct In alloys under the influence of thermosolutal melt convection, Met Mater Trans A. 44A (2013) 3797–3808.

[17] T. Anderson, I. Ansara, The Ga–In(gallium–indium) system, J. Phase Equilibria. 12 (1991) 64–72.

[18] W. Tyson, W. Miller, Surface free energies of solid metals: Estimation from liquid surface tension measurements, Surf. Sci. 62 (1977) 267–276.

[19] P.A. Savintsev, A.A. Akhkubekov, K.A. Getazheev, V.I. Rogov, V.S. Savvin, Determination of diffusion coefficients and activity rates for gallium-indium system by contact melting method, Sov Phys J. (1971) 53-.

[20] H. Neumann-Heyme, K. Eckert, C. Beckermann, General evolution equation for the specific interface area of dendrites during alloy solidification, Acta Mater. 140 (2017) 87–96.

[21] J.J. Reeves, T.Z. Kattamis, Model for isothermal dendritic coarsening, Scr. Met. Mater. 5 (1971) 223-.

[22] J. Zhang, S.O. Poulsen, J.W. Gibbs, P.W. Voorhees, H.F. Poulsen, Determining material parameters using phase-field simulations and experiments, Acta Mater. 129 (2017) 229–238.

[23] H.-J. Diepers, C. Beckermann, I. Steinbach, Simulation of convection and ripening in a binary alloy mush using the phase-field method, Acta Mater. 47 (1999) 3663–3678.

[24] J.A. Dantzig, M. Rappaz, Solidification, EPFL Press, 2009.

[25] W.F. Gale, T.C. Totemeier, Smithells Metals Reference Book, Butterworth-Heinemann, 2003.